

The growth and characterisation of Ni₅Zn₂₁ dendrites

Lang Qin · Jun Zhang · Tiehan H. Shen ·
Grenville A. Jones · Eun-Sang Choi ·
Yong-Jie Wang · Chris Binns

Received: 18 September 2009 / Accepted: 21 November 2009 / Published online: 5 December 2009
© Springer Science+Business Media, LLC 2009

Abstract We have investigated the growth of Ni–Zn alloys by a dc electrodeposition method and a pulse dc electrodeposition method with different pulse frequencies, under otherwise the same growth conditions. Dendritic growth is found in the Ni–Zn alloys produced by pulse dc electrodeposition, whereas such growth is absent in those fabricated by dc electrodeposition. The morphology of the as-grown Ni–Zn dendrites is highly influenced by the pulse frequency. The possible growth mechanism has been discussed. The corresponding magnetic properties are investigated at 5 K using a superconducting quantum interference device. We have observed a clear variation in the magnetisation behaviour as the pulse frequency is changed, which is likely to be attributable to the presence of precipitation of Ni nanoparticles.

Introduction

The latest research has demonstrated that an alloy of Ni–Zn (with a high percentage of Zn) has promising potential applications in the catalyst industry. Studt et al. [1] have calculated the adsorption energies of reactants and intermediates and used that analysis to identify a descriptor for

both catalytic activity and selectivity. They singled out Ni–Zn alloys as the most promising candidate because not only is the production cost lower, but they also exhibit good catalytic activity and even greater selectivity than Pd–Ag catalysts in certain chemical processes. Moreover, a recent study suggests that dendritic alloys have enhanced electrocatalytic activity [2]. This makes dendritic growth of Ni–Zn a subject of interest.

Currently, electrodeposition is one of the commonest methods used for the preparation of metals and alloys [3]. Recent studies indicate that the deposition conditions such as bath composition [4], electrolyte concentration [5] and waveform of the deposition current [6] exhibit a strong effect on the grain size and morphology of electrodeposited metals or alloys. On the other hand, it has been demonstrated that similar effects can be achieved by applying pulse electrodeposition with other conditions remaining unchanged [7]. In the present investigation, we report the fabrication of Ni–Zn alloys in the form of quasi two-dimensional hexagonal shaped platelets or three-dimensional dendrites. In each case these were grown by pulse dc electrodeposition on an aluminium surface. An investigation of the morphology of these alloys has been undertaken. Potential mechanisms responsible for the dendrite growth are discussed within the existing theoretical frameworks [8–14].

Experimental

The electrodeposition was carried out in a cubical shaped cell containing 100 mL of electrolyte solution. The cathode was a piece of graphite of about 6 cm² surface area. The anode, also serving as a substrate, was a piece of 1 cm × 1 cm aluminium sheet (purity 99.999%), which

L. Qin · J. Zhang · T. H. Shen (✉) · G. A. Jones
Joule Physics Laboratory, University of Salford, Salford
M5 4WT, UK
e-mail: t.shen@salford.ac.uk

E.-S. Choi · Y.-J. Wang
NHMFL FSU, 1800 E. Paul Dirac Dr., Tallahassee,
FL 32310-370, USA

C. Binns
Department of Physics and Astronomy, University of Leicester,
University Road, Leicester LE1 7RH, UK

had been electropolished at a constant voltage of 18.0 V in a mixture of perchloric acid (HClO_4) and ethanol ($v_{\text{HClO}_4} : v_{\text{ethanol}} = 1 : 4$). Prior to fabrication, the electrodes were rinsed with de-ionized water. The Ni–Zn alloy deposition was conducted at room temperature in an electrolyte prepared using de-ionised water and analytical grade reagents containing ZnCl_2 (0.5 M), $\text{NiSO}_4 \cdot 6\text{H}_2\text{O}$ (0.05 M), and a H_3BO_3 buffer (an electrolyte with a pH value 3). The growth was conducted at a peak voltage of -4.0 V by the pulse dc method [15] using a square waveform (i.e. equal on/off periods, $T_{\text{on}} = T_{\text{off}}$) and a pulse frequency of 25, 500 or 1,000 Hz. Also, dc electrodeposition at an applied voltage of 4.0 V was used with all the other experimental conditions unchanged. After deposition, the samples were immediately washed with de-ionised water and dried in air.

The structures of as-deposited Ni–Zn alloys were determined by XRD using Cu $K\alpha$ radiation ($\lambda = 0.15405$ nm). The alloy composition was further examined by energy-dispersive X-ray spectroscopy (EDS) and the morphology by scanning electron microscopy (SEM) at an accelerating voltage of 30 kV. Samples for TEM were physically removed from the substrate and ultrasonically dispersed in ethanol and drop cast on TEM carbon-coated copper grids. The magnetisation characteristics were measured between $-10,000$ and $10,000$ Oe at 5 K using a superconducting quantum interference device (SQUID) magnetometer.

Results and discussion

An XRD spectrum of the aluminium substrate is shown in Fig. 1a; the three strongest peaks can be identified as the (200), (220) and (311) reflections of aluminium (JCPDF-85-1327). In Fig. 1b is shown the XRD spectrum taken from Ni–Zn alloy samples deposited at 25 Hz with $T_{\text{on}} = T_{\text{off}} = 20$ ms. The three peaks can be assigned to diffraction from the (330), (600) and (633) planes of $\text{Ni}_5\text{Zn}_{21}$, which has a known body centred cubic (bcc) structure (JCPDF No. 10-0209). In fact, the XRD spectrum of Fig. 1b is typical of all the as-grown Ni–Zn samples, regardless of the pulse frequency used. This may be explained by the fact that the XRD results reveal structural information about an entire film, whereas the dendritic structures occur only on the upper surface of a sample. The composition of the alloys was checked by EDS and confirmed a nominal atomic ratio of Ni to Zn of 5:21.

Though the crystalline phase of the alloys is independent of pulse frequency, it is not the case for alloy morphology. Figure 2a shows an SEM image of a $\text{Ni}_5\text{Zn}_{21}$ alloy sample deposited at 1,000 Hz with $T_{\text{on}} = T_{\text{off}} = 0.5$ ms. It comprises an assembly of randomly arranged platelets. The

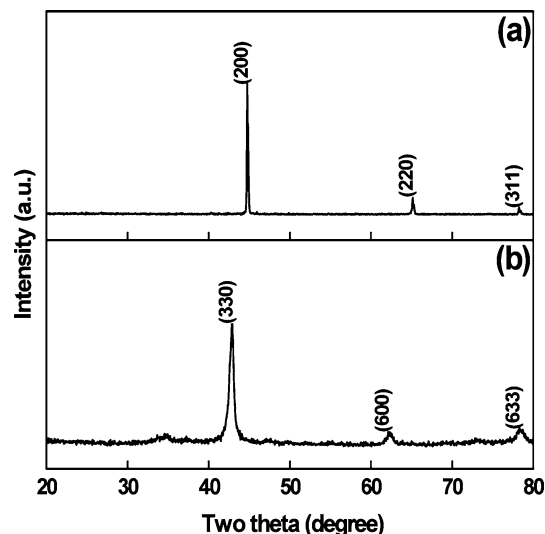


Fig. 1 XRD patterns of **a** aluminium substrate and **b** Ni–Zn alloy electrodeposited at 25 Hz

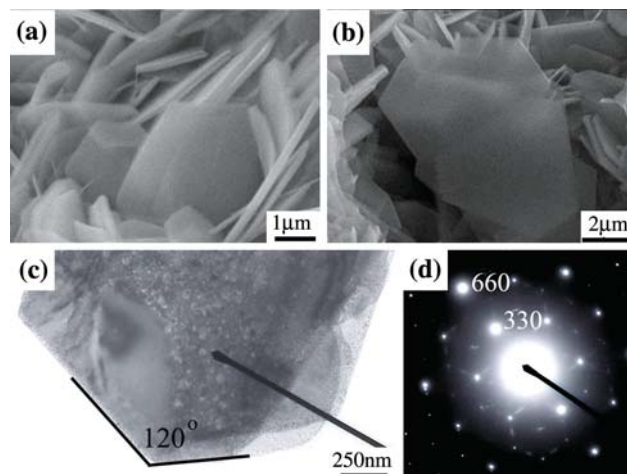


Fig. 2 $\text{Ni}_5\text{Zn}_{21}$ hexagonal platelets electrodeposited at 1,000 Hz. **a** Side view of a group of platelets, **b** plan view of platelets, **c** TEM image taken from a section of platelet and **d** its SAED pattern

platelets have an average thickness in the range 100–200 nm while the ‘long’ dimension is from 2 to 3 μm . Individual platelets frequently display a hexagonal shape; an example is shown in Fig. 2b. This result is consistent with the TEM observation. Figure 2c is a TEM micrograph of a single platelet in which facets at an angle of 120° are clearly visible. The associated SAED pattern (Fig. 2d) proves that the platelet is monocrystalline and that the reduced dimension is parallel to a $\langle 111 \rangle$ axis. The six ‘spots’ closest to the centre of the pattern can be indexed as $(\bar{3}30)$, $(\bar{3}03)$, $(0\bar{3}3)$, $(3\bar{3}0)$, $(30\bar{3})$ and $(03\bar{3})$.

The dendrites formed at a pulse frequency of 500 Hz with $T_{\text{on}} = T_{\text{off}} = 1$ ms are observed by SEM. In Fig. 3a is shown a spine-like dendrite. Figure 3b, c displays the side

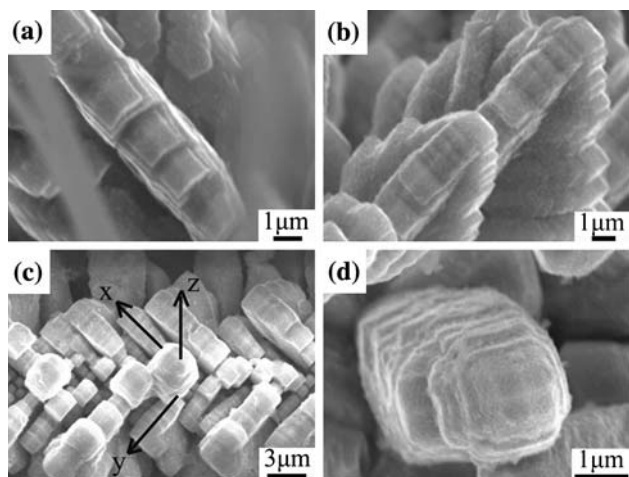


Fig. 3 $\text{Ni}_5\text{Zn}_{21}$ deposited at a pulse frequency of 500 Hz: **a** a bamboo-like structured unit, **b** side view and **c** plan view of a group of these units growing along three x , y , and z axes of Cartesian coordinate system, **d** a $\text{Ni}_5\text{Zn}_{21}$ unit with a cross on top

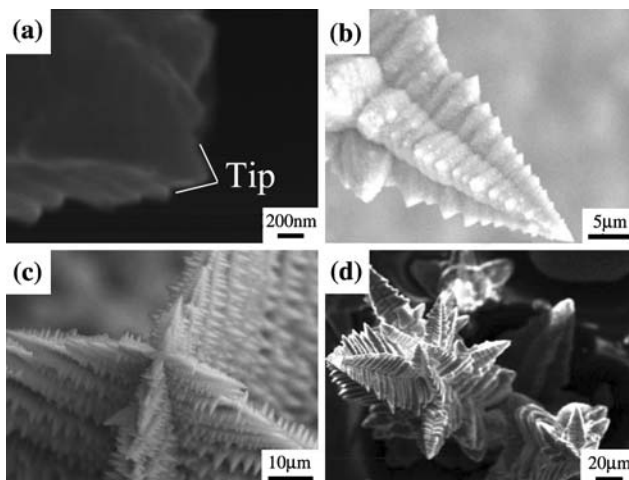


Fig. 4 $\text{Ni}_5\text{Zn}_{21}$ alloy deposited at a pulse frequency of 25 Hz: **a** sharp tip, **b** a unit, **c** top view, **d** clusters of $\text{Ni}_5\text{Zn}_{21}$ dendrites

view and the plan view of a group of these dendrites growing along the three x , y , and z axes of the Cartesian coordinate system, respectively. A cross on the top of a segment dendrite is shown in Fig. 3d. The crosses are common on external surface of dendrites in this set of samples, suggesting a dendritic growth direction of $[100]$, which will be discussed in the following text.

By comparison, the morphology of $\text{Ni}_5\text{Zn}_{21}$ alloys electrodeposited at 25 Hz is shown in Fig. 4. One can see that only four-fold symmetric dendrites grow under this condition. An image of the dendrite unit is shown in Fig. 4b. Hundreds of these units form an orthogonal branch and the angles of the branches with respect to the main trunk are all about 90° (Fig. 4c). Finally, an extended structure of dendrites is observed (Fig. 4d). It is also

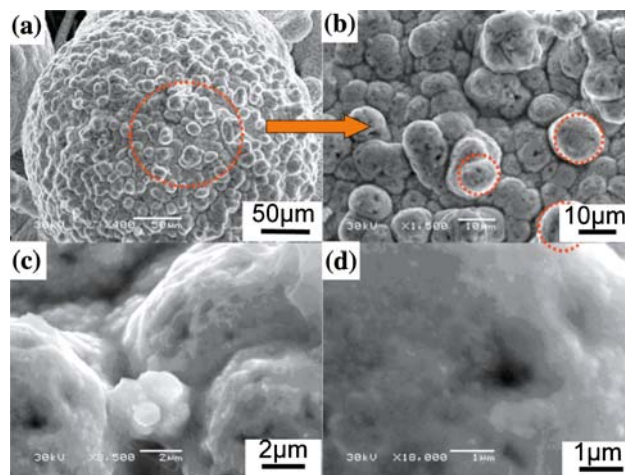


Fig. 5 $\text{Ni}_5\text{Zn}_{21}$ alloys deposited by dc electrodeposition. SEM images of sample surface with magnification **a** $\times 400$, **b** $\times 1,500$, **c** $\times 8,500$ and **d** $\times 18,000$

notable that the ends of each branch tend to form extremely sharp tips of less than 100 nm (Fig. 4a), which provides these sets of samples with potential application as probes in scanning probe microscopy. During the formation of a dendrite at 25 Hz with a relaxation time of 20 ms, the secondary branches will grow perpendicular to the primary trunk and smaller twigs perpendicular to a branch. From this morphological characterisation, we see that the growth of $\text{Ni}_5\text{Zn}_{21}$ dendrites takes place along three orthogonal directions. One direction is the main growth direction along $[100]$ and, within a plane normal to this main direction, each growth unit extends itself along the four directions of $\langle 001 \rangle$.

For reference, $\text{Ni}_5\text{Zn}_{21}$ alloys produced by dc electrodeposition are also investigated in terms of their morphology. Spheres with a diameter of $300 \mu\text{m}$ predominate in these samples (Fig. 5a). Each sphere is composed of hundreds of grains; a few are circled by a dashed line. The average diameter of the grains is about $10 \mu\text{m}$ with a variation of $5 \mu\text{m}$ (Fig. 5b). The surfaces of these grains are rough (Fig. 5c, d) without any dendritic structures.

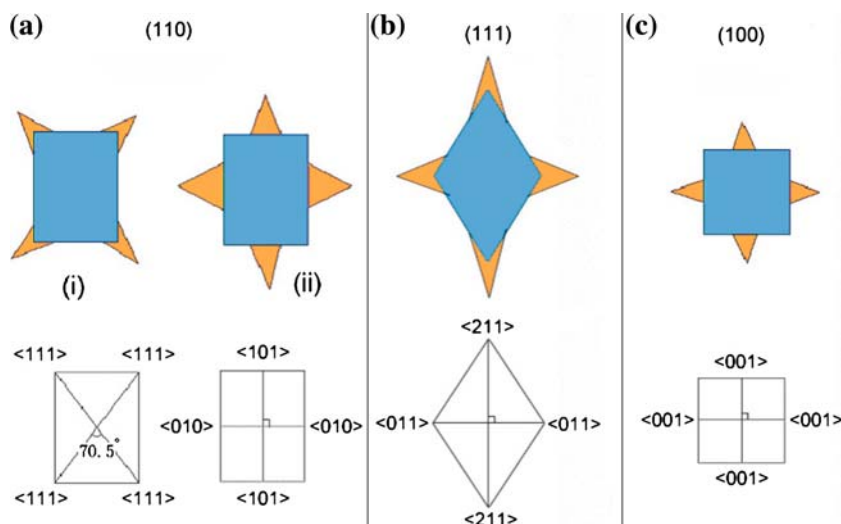
The co-reduction of zinc and nickel ions leading to the formation of Ni–Zn alloys can be written as



In the $\text{Ni}_5\text{Zn}_{21}$ alloys deposited at 25 and 500 Hz, it is difficult to obtain clear TEM images or SAED patterns because the sample structures are too thick to be examined. Nevertheless, the formation of four-fold symmetric limbs can be explained by the supposition that the crystal growth along two certain orthogonal directions is faster than the other directions.

Now we analyse the possible growth directions of $\text{Ni}_5\text{Zn}_{21}$ dendrites deposited at 25 and 500 Hz. In a bcc

Fig. 6 Possible growth directions of bcc dendrites



crystal, the three most common crystal faces are (110), (111) and (100) planes, as illustrated in Fig. 6a, b and c, respectively. In case (a), the branch units grow in the (110) plane: in (i) they extend along $\langle 111 \rangle$ directions or in (ii) they extend along $\langle 101 \rangle$ and $\langle 010 \rangle$ directions. In case (i), the angles between the limbs are 70.5° or 109.5° , which are different from the 90° angles observed in $\text{Ni}_5\text{Zn}_{21}$ dendrites. For case (ii), the dendrites grow orthogonally along $\langle 101 \rangle$ and $\langle 010 \rangle$ directions but probably not at an equal rate on account of different surface energies, which makes symmetric growth impossible. In case (b), the possible limbs develop along $\langle 211 \rangle$ and $\langle 011 \rangle$, which also will not lead to symmetric dendrite growth. In case (c), the branch units intersect orthogonally along $\langle 001 \rangle$ directions, which makes the protrusion of four branches isoenergetic. Thus, we can draw the conclusion that $\langle 001 \rangle$ is the preferential growth direction and that the crosses found in samples deposited at 500 Hz may be adduced as direct evidence. Dendritic growth is believed to occur under non-equilibrium conditions, which are not necessarily the most stable in terms of surface energy [16–19]. This suggests that a change in pulse frequency might affect the surface kinetics.

Though the mechanism of pulse dc electrodeposition is not yet fully understood, its impact on crystal morphology is significantly different from that of dc electrodeposition. The current density at which dendrite crystals begin to form is defined as the limiting current density (j_L). At this current density, the ion concentration at the deposited surface is zero. Pulse electrodeposition can raise j_L considerably in comparison with dc electrodeposition because the deposited metal ions of the cathode surface can be supplied from the bulk solution during the off-period (T_{off}) of the pulse.

Ibl [20] stated that the ratio of $T_{\text{on}}/T_{\text{off}}$ can be an important factor because the properties of metal deposits

can be influenced by both the on-time, during which formation of nuclei and growth of existing crystals occur, and the off-time, during which desorption of deposited ions takes place.

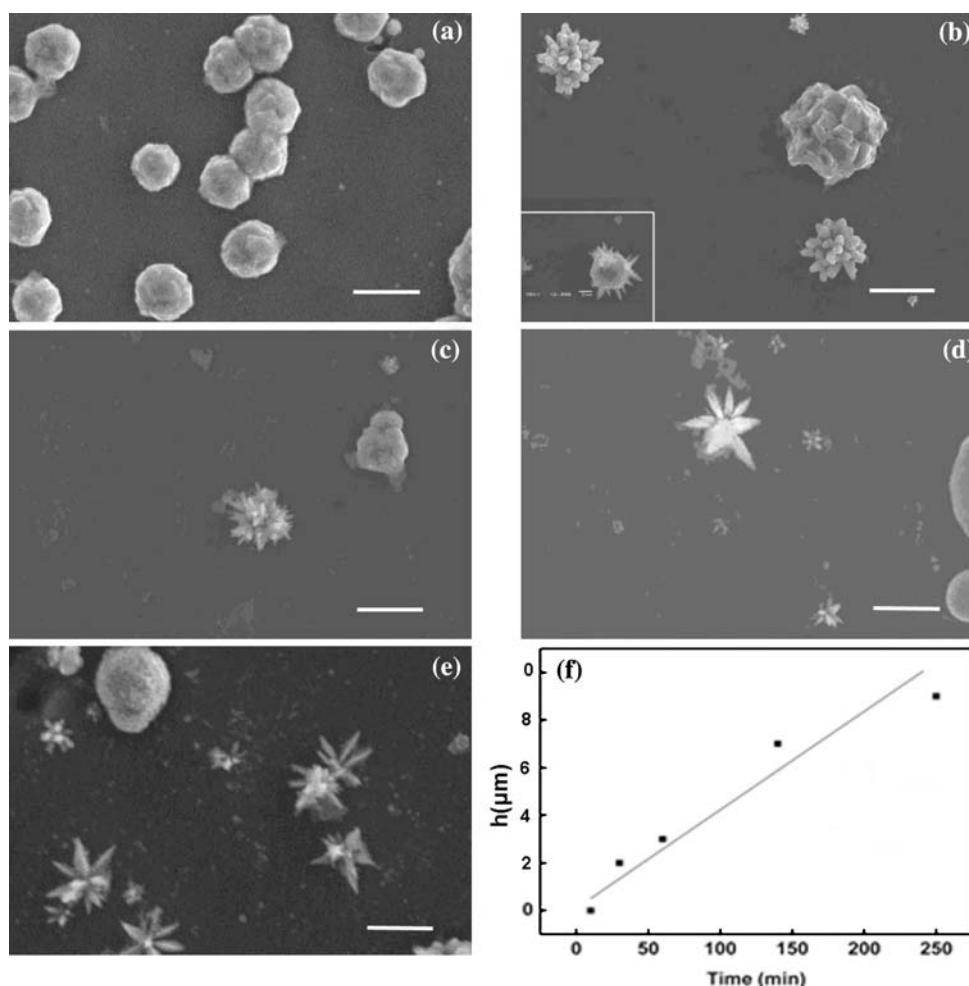
In the first place, we may explain the morphological differences of the alloys obtained by dc electrodeposition and pulse dc electrodeposition (pulse frequency = 25, 500 or 1,000 Hz) based on the different rate of nuclei formation, which itself depends on the overpotential. The rate of nuclei formation (γ) is related to the overpotential (η) [21]:

$$\gamma = k_1 \exp(-k_2/\eta^2), \tag{2}$$

where k_1, k_2 are constants. Under the same applied voltage, the overpotential of pulse dc electrodeposition is larger than that of dc electrodeposition by $\eta_o \ln \left(\frac{T_{\text{on}}}{T_{\text{on}} + 1} \right)$, where η_o is the overpotential at the exchange current density (j_o) [22]. This implies that dendritic growth is favoured in pulse dc electrodeposition, which possesses a higher overpotential. Taking into account the surface energy of the alloys, the overpotential of Ni–Zn dendrites deposited at 25, 500 and 1,000 Hz may be different, which results in the different rate of nuclei formation, hence a change in morphology of the deposits.

The average growth rate of dendrites was measured in samples deposited at 25 Hz; the SEM images of dendrites deposited at different time are shown in Fig. 7a–e. Within a deposition time of 10 min, $\text{Ni}_5\text{Zn}_{21}$ alloys grow in the form of spheres with an average size of 8 μm (Fig. 7a). The branches of the dendrites start to develop in a deposition time of 10–30 min (Fig. 7b). The tips of the dendrites become much sharper when the deposition time is increased to 60 min (Fig. 7c). More dendrites can be found after a deposition of 140 min (Fig. 7d) and their average height continues to increase (Fig. 7e). The change of average height is given by [23]:

Fig. 7 SEM images of dendrites grown at **a** 10 min, **b** 30 min, **c** 60 min, **d** 140 min and **e** 250 min and **f** the time-dependence of the average height of dendrites. Scale bar = 10 μm



$$\frac{dh}{dt} = j_0 \frac{V}{zF} \left[1 - \exp\left(\frac{2(1-\beta)\sigma V}{RT r}\right) \right], \quad (3)$$

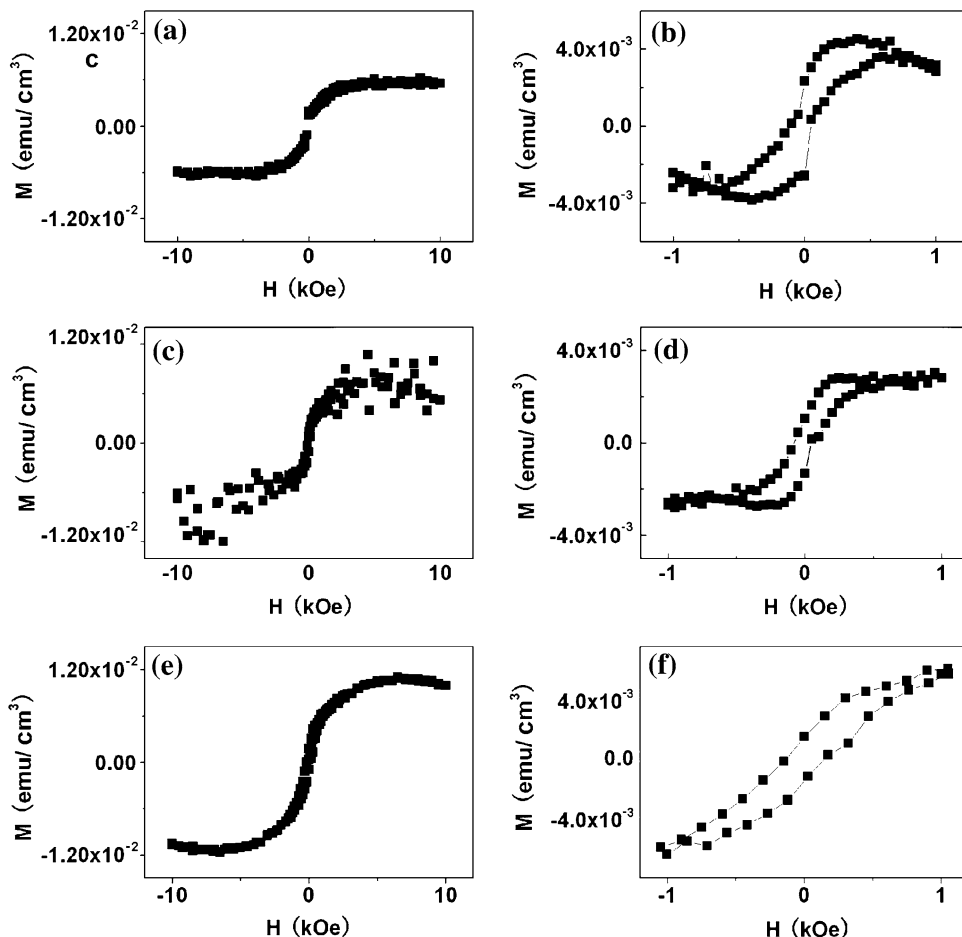
where h is the average height of surface protrusions with tip radius r , t the time, V the molar volume, z the number of electrons, F the Faraday constant, R the gas constant, T the temperature, β the symmetry factor and σ the surface energy. One can see that h increases linearly with deposition time as all the parameters in Eq. 3 are constant under the experimental conditions. The average height as a function of time is shown in Fig. 7f, a clear linear relation can be found. Consequently, one can draw the conclusions that (i) the dendrites start to grow after a deposition time of 10 min and (ii) the growth rate of a dendrite is constant at $0.42 \pm 0.07 \mu\text{m}/\text{min}$.

Alloys with Zn composition higher than 20 atom.% are known to be non-ferromagnetic at room temperature [24]. It is difficult to predict the magnetic behaviour of Zn–Ni alloys at lower temperatures. In this work, hysteresis loops were measured by SQUID between $-10,000$ and $+10,000$ Oe at 5 K. Weak ferromagnetic behaviour was found in all three

sets of samples. Samples fabricated at 1,000 Hz have a saturation magnetisation of $5.6 \times 10^{-3} \text{ emu}/\text{cm}^3$ (Fig. 8a) with an estimated coercivity of 40 Oe (Fig. 8b). The coercivity and saturation magnetisation tend to increase as the pulse frequency of deposition increases, i.e. the coercivity is 75 Oe in samples deposited at 500 Hz (Fig. 8d), whilst it is 150 Oe at 25 Hz (Fig. 8f). Similarly, the saturation magnetisation is $7.2 \times 10^{-3} \text{ emu}/\text{cm}^3$ (Fig. 8c) and $1.09 \times 10^{-2} \text{ emu}/\text{cm}^3$ (Fig. 8e) in samples deposited at 500 and 25 Hz, respectively.

In their recent work, Liu et al. [25] suggested that the unavoidable existence of Ni-rich ‘microzones’ in their as-prepared $\text{Ni}_5\text{Zn}_{21}$ nanowires gave rise to weak ferromagnetic characteristics. In this work, we may also explain the magnetism under the assumption of unalloyed Ni nanograins. The total volume of $\text{Ni}_5\text{Zn}_{21}$ alloy (v_{NZ}) is 0.0020 cm^3 and the total volume of Al substrate (v_{A}) is 0.025 cm^3 . Assuming that Ni exists in the form of particles in all the as-deposited samples, the total volume of Ni particles is v_{N} . Thus, the percentage of Ni particles in the Ni–Zn alloys is given by:

Fig. 8 *M–H* loops of Ni₅Zn₂₁ samples deposited at **a–b** 1,000 Hz, **c–d** 500 Hz and **e–f** 25 Hz. All measured at 5 K



$$\frac{v_N}{v_N + v_{NZ}} = \frac{M_N v_{NZ} + M_N v_A}{M_N v_{NZ} + M_{SN} v_{NZ}} \tag{4}$$

where the saturation magnetisation of bulk Ni (M_{SN}) is 487 emu/cm³ at 5 K [26] and M_N is the saturation magnetisation of Ni–Zn alloys obtained from Fig. 8.

Using Eq. 4, the volume fraction of Ni particles to Ni–Zn alloy can be estimated in all three sets of products. They are approximately 0.016, 0.020 and 0.030 vol.% in the samples produced by the pulse frequency of 1,000, 500 and 25 Hz, respectively. The difference in saturation magnetisation value among these three sets of samples could be attributed to the quantity of Ni grains by electrodeposition at different pulse frequencies. This would suggest that the dendrites are Ni doped alloys with the composition of Ni₅Zn₂₁ higher than 99.9%. Thus, it is difficult to examine the extra Ni grains by SAED, XRD or EDS.

Conclusion

To summarise, Ni–Zn platelets and dendritic structures are fabricated by dc and pulse dc electrodeposition. The three sets of Ni₅Zn₂₁ samples show an identical bcc crystal

structure; however, their morphology is different. Hexagonal Ni platelets are produced in the samples deposited at the pulse frequency of 1,000 Hz, whereas bamboo-like structures and flower-like dendrites are obtained at 500 and 25 Hz, respectively. We confirmed that the dendrites started to grow after a deposition time of 10 min with a growth rate of $0.42 \pm 0.07 \mu\text{m}/\text{min}$. The detectable ferromagnetic behaviour at low temperatures suggests the existence of Ni nanograins. The volume percentage of Ni nanograins to total Ni–Zn alloy is estimated to be 0.016, 0.020 and 0.030 vol.% in the samples produced by the pulse frequency of 1,000, 500 and 25 Hz, respectively. The Ni–Zn platelets/dendrites may exhibit promising catalytic behaviour, which is the subject of our future work.

Acknowledgements We wish to thank Prof. P. J. Grundy for his interest in this work as well as useful discussions. Both L.Q. and J.Z. would like to acknowledge the ORSAS and the University of Salford for their scholarships.

References

1. Studt F, Abild-Pedersen F, Bligaard T, Sørensen RZ, Christensen CH, Nørskov JK (2008) Science 320:1320
2. Wang J, Thomas DF, Chen A (2008) Chem Commun 31:5010

3. Manhabosco TM, Muller IL (2009) *J Mater Sci* 44:2931. doi: [10.1007/s10853-009-3388-9](https://doi.org/10.1007/s10853-009-3388-9)
4. Mishra AC, Thakur AK, Srinivas V (2009) *J Mater Sci* 44:3520. doi: [10.1007/s10853-009-3475-y](https://doi.org/10.1007/s10853-009-3475-y)
5. Lee HM, Mahapatra SK, Anthony JK, Rotermund F, Kim CK (2009) *J Mater Sci* 44:3731. doi: [10.1007/s10853-009-3498-4](https://doi.org/10.1007/s10853-009-3498-4)
6. Xu JX, Xu Y (2008) *J Mater Sci* 43:4163. doi: [10.1007/s10853-006-1222-1](https://doi.org/10.1007/s10853-006-1222-1)
7. Li L, Li G, Zhang Y, Yang Y, Zhang L (2004) *J Phys Chem B* 108:19380
8. Fleury V (1997) *Nature* 390:145
9. Ní Mhíocháin TR, Hinds G, Martin A, Chang EZY, Lai A, Costiner L, Coey JMD (2004) *Electrochim Acta* 49:4813
10. Grier D, Ben-Jacob E, Clarke R, Sander LM (1986) *Phys Rev Lett* 56:1264
11. Fleury V (2000) *Phys Rev E* 61:4156
12. Chazalviel JN (1990) *Phys Rev A* 42:7355
13. Argoul F, Kuhn A (1995) *Physica A* 213:209
14. Argoul F, Freysz E, Kuhn A, Leger C, Potin L (1996) *Phys Rev E* 53:1777
15. Zhang J, Jones GA, Shen TH, Donnelly SE, Li G (2007) *J Appl Phys* 101:054310
16. Chernov AA (1974) *J Cryst Growth* 11:24
17. Kuroda T, Irisawa T, Ookawa A (1977) *J Cryst Growth* 41:42
18. Berg WF (1938) *Proc R Soc Lond* 79:A164
19. Mullins WW, Sekerka RF (1963) *J Appl Phys* 34:323
20. Ibl N (1980) *Surf Technol* 10:81
21. Toshev S, Markov I (1967) *Electrochim Acta* 12:281
22. Choi KH, Kim HS, Lee TH (1998) *J Power Sources* 75:230
23. Popov KI, Maksimovic MD (1989) *Mod Aspects Electrochem* 19:193
24. Hanson M (1958) *Constitution of binary alloys*, 2nd edn. McGraw-Hill, New York
25. Liu L, Tian H, Xie S, Zhou W, Mu S, Song L, Liu D, Luo S, Zhang Z, Xiang Y, Zhao X, Ma W, Shen J, Li J, Wang C, Wang G (2006) *J Phys Chem B* 110:20158
26. Gray ED (1972) *American institute of physics handbook*. McGraw-Hill, New York